On the importance of FIB-SEM specific segmentation algorithms for porous media

Martin Salzer[a,*], Simon Thiele[b], Roland Zengerle[b], Volker Schmidt[a]

(martin.salzer@uni-ulm.de, simon.thiele@imtek.uni-freiburg.de,

zengerle@imtek.uni-freiburg.de, volker.schmidt@uni-ulm.de)

[a] Institute of Stochastics, Faculty of Mathematics and Economics,

Ulm University, D-89069 Ulm, Germany

[b] Laboratory for MEMS Applications, IMTEK – Department

of Microsystems Engineering, University of Freiburg,

D-79110 Freiburg, Germany

[*] Corresponding author. Phone +49 (0)731/50-23555,
Fax: +49 (0)731/50-23649.

Abstract

A new algorithmic approach to segmentation of highly porous three dimensional image data gained by focused ion beam tomography is described which extends the key-principle of local threshold backpropagation described in [1]. The technique of focused ion beam tomography has shown to be capable

of imaging the microstructure of functional materials. In order to perform a quantitative analysis on the corresponding microstructure a segmentation task needs to be performed. However, algorithmic segmentation of images obtained with focused ion beam tomography is a challenging problem for highly porous materials if filling the pore phase, e.g. with epoxy resin, is difficult. The grey intensities of individual voxels are not sufficient to determine the phase represented by them and usual thresholding methods are not applicable. We thus propose a new approach to segmentation, that pays respect to the specifics of the imaging process of focused ion beam tomography. As an application of our approach, the segmentation of three dimensional images for a cathode material used in polymer electrolyte membrane fuel cells is discussed. We show that our approach preserves significantly more of the original nanostructure than an thresholding approach.

Keywords: 3D Imaging, FIB-SEM Tomography, Porous Media, Segmentation

---

1. Introduction

In the next decades humanity has to face the problem of global climate change which is linked to our societies present and future energy consumption. Replacing fossil fuels and internal combustion engines by hydrogen and fuel cells is regarded as a key solution for future sustainable energy supply [2]. In particular, polymer electrolyte membrane fuel cells (PEMFC) are important energy converters delivering electric energy from chemical energy. In the PEMFC reaction, hydrogen and oxygen are converted to water. For a controlled performance of this reaction a high level of technological know-how especially in the membrane electrode assembly (MEA) is mandatory [3]. This approximately 40 μm thick structure consists of an anode catalyst layer, a polymer electrolyte membrane (PEM) and a cathode catalyst layer (CCL). In the anode catalyst layer hydrogen molecules are catalytically split into electrons and protons. The PEM conducts protons to the anode but does not conduct electrons. The electrons can be conducted to the CCL via an electric circuit thereby providing electric energy. Finally, in the CCL, the protons, electrons and oxygen have to be transported to platinum catalyst sites where the crucial oxygen reduction reaction takes place.

There is no doubt that the 3D CCL morphology has a large impact on

the performance of PEMFCs [4]. To better understand the influence of CCL morphology on rate limiting processes, several approaches have been developed to create artificial CCL morphologies [5]. However, since the CCL morphology is considerably influencing the transport processes within PEMFC, methods are required for the correct reconstruction of real CCL morphologies in 3D. The method which is currently best suited for this purpose is Focused Ion Beam (FIB) / Scanning Electron Microscope (SEM) tomography (shortly called FIB-SEM tomography in this paper). Note that FIB-SEM tomography is an advanced imaging technique which has successfully been used in materials science, e.g. for ceramics [6, 7], batteries [8, 9] and PEMFC cathodes [10, 11]. But algorithmic segmentation of FIB-SEM images is a challenging problem for highly porous materials especially if it is difficult to fill the pore phase, e.g. with epoxy resin. Due to the principle of serial sectioning, images of porous media contain a specific type of shine-through artefacts. They appear when the xy sectioning plane intersects with pore space. The gray-values then represent the solid material behind the pore instead of the (empty) pore space itself. As a consequence image characteristics are similar to those of other parts of the image that do not cover pore space. Therefore the gray-value itself is not a sufficient, and sometimes even misleading,

criteria for classification of individual voxels. The quality of the obtained segmentation, however, has a direct impact on how meaningful a later analysis of the obtained microstructure will be. In [12], e.g., the authors observe significant difference in porosity for different segmentation approaches. We believe that this due to the fact that the studied algorithms are general purpose methods and do not consider the specific nature of FIB-SEM images as mentioned above.

We thus propose a different approach to segmentation of FIB-SEM images, which is an extension of an algorithm recently introduced in [1] for the segmentation of FIB-SEM images of another type of porous material.

In the present paper, our algorithm is applied to FIB-SEM images for CCL material, where we detect the first and last occurrences of individual substructures by analysing the variation of grey intensities in z-direction. This idea is inspired of the way images are obtained by FIB-SEM tomography and seeks to eliminate shine-through artefacts as mentioned above. The algorithm is validated by comparing its segmentation results with those obtained by thresholding methods and by a manual segmentation approach [11], which is both subjective and time consuming. Besides that we apply our algorithm to an additional data sample, which serves as a validation for

its flexibility and its potential to work for different scenarios.

The paper is organized as follows. In Section 2, we describe the material and image data that is used as an example of application of our approach. In the following Section 3 we introduce our method of automatic image segmentation. In Section 4, we discuss the obtained segmentation results and compare them to those which have been received by global thresholding and manual segmentation, respectively. Finally, in Section 5 we provide a conclusion and give an outlook to possible future research.

2. Preliminaries

2.1. Description of Material and Imaging Technique

In this study, a pristine commercial Gore PRIMEA A510.1 M710.18 C510.4 PEMFC membrane electrode assembly was used to carry out all tomographic experiments, see Fig. **??**a. For this material, water modeling and imaging techniques complementary to FIB-SEM tomography have been studied e.g. in [8, 13] but without establishing any automatic image segmentation. The analysis was performed by a Zeiss 'Neon 40EsB' with a x- and y resolution of 2.5 nm and a cutting distance of 13.6 nm in z-direction.

The loading which is mass of Pt per surface area was 0.1 mg/cm^2 at the

anode and 0.4 mg/cm^2 at the cathode. The CCL has a thickness of about 11 μm while the thickness of the anode catalyst layer is about 3.5 μm.

For FIB-SEM tomography a FIB for cutting and an SEM for the imaging are positioned in an angle of 50°–54°. With the FIB, gallium ions are accelerated towards the surface of the investigated sample provoking a very local sputtering process with spot sizes of 10 nm and less. The FIB thereby enables to remove slices from the sample, see Fig. **??**b. Successive slicing by the FIB and image acquisition by the SEM produces a stack of 2D images.

It is important to note, that for porous media each 2D slice does not only show structures located in that particular plane. Instead structures that are located behind a pore are visible much earlier.

2.2. Preprocessing

Due to the different angles of the FIB and the SEM the obtained images contain a significant drift in y-direction that increases in z-direction. Correcting this drift is essential, as the algorithm described below strongly relies on correct alignment.

To accomplish this, we used a modified version of the least-square difference algorithm described in [14]. The algorithm determines the vector that leads to the smallest difference between two images when they are shifted

in the direction of the vector. We modify this approach by only accounting voxels below a certain threshold ($\tau_{\text{shift}} = 75$). This guarantees that the alignment is computed based on the background structures we try to detect later on. Additionally, we use linear interpolation to estimate grey intensities for values of non-integral coordinates. The drift is then determined by computing the difference between slice z and its successor $z + 1$ for all shift vectors $(s_x, s_y) \in \{-10, -9.5, -9, \ldots, 9.5, 10\}^2$ where we determine the shift vector that leads to the minimal difference. Finally, we apply a 2D mean value filter with radius $r = 1.0$ to the image.

2.3. Basic Notation

We denote by I the preprocessed image obtained by FIB-SEM tomography as described above, where I is a function that maps each voxel location (x, y, z) to its corresponding grey intensity $I(x, y, z)$, also denoted by $I_{xy}(z)$ in the following.

3. Image Segmentation

In this section we present a new approach to segmentation of FIB-SEM images. This approach extends the key-principle of local threshold backpropagation described in [1]. There, we detected sudden drops in grey intensity

for given x and y coordinates and stepwise increasing z-values. We then used the last grey intensity before the drop to estimate a reasonable threshold that was used to detect the beginning of the currently visible structure. This idea, however, was based on the assumption that grey intensities remain the same within each substructure (while different substructures may have different grey values). However, this assumption does not hold for all datasets in particular not for the currently analyzed one: For many substructures we find a huge variation of the grey intensity. This is caused by the geometry of the structure and by various properties of its material. Both of which have an impact on the grey intensity. For example rough surfaces lead to higher grey intensities than surfaces with similar properties that are smoothed by the sputtering effect of the FIB. Additionally, there is a shine-through effect for thinner structures, which appear semi-transparent, i.e. they have a lower grey intensity in the image. The sum of these influences results in a dataset where neither global nor common local thresholding schemes lead to sufficiently good results. Even more advanced techniques like the approach presented in [1] are not able to cover the complexity of the given data. Therefore we developed a new approach the basic idea of which is given below. For a general overview of the presented approach including the tasks concerning

pre- and postprocessing, see the flow chart in Fig. **??**.

3.1. Segmentation Principle

For any given pair (x, y) we consider the 1D restriction I_{xy} of the image I. Within this image we detect both phase shifts, i.e. the first and the last occurrence of a substructure, by looking for local maxima and minima, respectively. This is based on the following heuristic principle: When a substructure is visible but still located in the background its grey intensity at this point is still relatively low. With each layer the FIB cuts off more electrons emitted from the background structures in the pores can be detected by the SEM detector. Thus the corresponding background intensities increase. This continues until the substructure reaches the active slice. Therefore, we assume the grey intensity to reach a local maximum at the substructure's first occurrence, see Fig. **??**. For the last occurrence of a substructure an analogous assumption is made. When a structure is being cut off by the FIB the pore space behind becomes visible. Due to the greater distance of the following substructure that is separated by the just recently revealed pore space, the corresponding grey intensity is supposed to be significantly lower. Thus, we assume to reach a local minimum after the last occurrence of a substructure.

This principle is based on the way images are obtained by FIB-SEM tomography, as described in Section 2.1. We do not rely on common criteria like the absolute (or relative) grey intensity or the local gradient, but only consider extrema in one, namely z-direction.

3.2. Detecting Local Extrema

We attempt to detect local minima and maxima within a 1D image I_{xy}, which we assume to be the last and first occurrence of a substructure, respectively. Due to the above described variations in grey intensity, we need to distinguish local extrema that represent the first or last occurrence of substructures from those that are based on variations on grey intensities within substructures. Therefore we introduce the following definitions for local extrema. We define that $I_{xy}(z)$ represents a *local minimum* if both of the following two criteria are met: 1) $I_{xy}(z) < I_{xy}(z+\Delta)$ for each $\Delta \in \{-1, 1\}$, and 2) $I_{xy}(z') - I_{xy}(z) > \tau_{\min}$, where $\tau_{\min}$ is a prechosen threshold and z' denotes the location of the last *weak* maximum defined by

$$z' = \max\{z' < z : \, I_{xy}(z') > \max\{I_{xy}(z'-1), I_{xy}(z'+1)\}\}\,.$$

Furthermore, we say that $I_{xy}(z)$ represents a *local maximum* if both of the following two criteria are met: 1) $I_{xy}(z) > I_{xy}(z+\Delta)$ for each $\Delta \in \{-1, 1, 2\}$,

and 2) $I_{xy}(z) - I_{xy}(z^*) > \tau_{\max}$, where $\tau_{\max}$ again is a prechosen threshold, but z^* now denotes the location of the last minimum as defined above.

Note that these definitions are not fully symmetric, but there are two major differences. First, the grey intensity at voxel z is not only tested against the intensity at $z \pm 1$ but also against $z + 2$. This is to compensate for the fact that the speed the grey intensity increases is significantly slower than the decrease we try to detect. Therefore, smaller measurement errors, e.g. induced by false alignment, can lead to premature local maxima. Testing it against one additional grey intensity prevents the detection of some of these artificial local maxima. The difference in the characterization of local minima and local maxima is also the reason why we use two different thresholds ($\tau_{\min}$ and $\tau_{\max}$) to check for significance. When detecting local minima it is useful to use a higher value for $\tau_{\min}$ to prevent within-structural variations from being classified as last occurrences. Local maxima, on the other hand, are ignored when they appear within a structure and therefore lower values for $\tau_{\max}$ can be used.

Second, the grey intensity of a local minimum is not compared to the last local maximum but instead to the last *weak* local maximum. As the grey intensity of a substructure may not be the same for all slices its grey intensity

at the first occurrence is not a reasonable point of reference. The last *weak* maximum is closer to the currently tested local minimum and therefore more likely to provide a reasonable grey intensity.

3.3. Description of the Algorithm

We now employ the concepts stated above to give a complete description of the algorithm. For every pair (x, y) perform the following steps:

1. Denote the first local minimum by b_{xy}^0.
2. Set k to 1.
3. Compute $a_{xy}^k = \min\{z > b_{xy}^{k-1} : z \text{ local maximum}\}$.
4. Compute $b_{xy}^k = \min\{z > a_{xy}^k : z \text{ local minimum}\}$. If no local minima are left set b_{xy}^k to $z_{\max} + 1$ where $z_{\max}$ denotes the highest possible z value.
5. If there are local maxima left, increase k by 1 and continue with step 3.

Every interval $[a_{xy}^k, b_{xy}^k - 1]$ now represents the estimated life span of a substructure and the resulting binary image is given by

$$B_{\text{extrema}}(x, y, z) = \begin{cases} 255\,, & \text{if } z \in \bigcup_{k=1}^{k_{xy}^{\max}} [a_{xy}^k, b_{xy}^k - 1], \\ 0\,, & \text{otherwise.} \end{cases}$$

3.4. Postprocessing

Due to the complex nature of FIB-SEM images the approach described above is not able to classify every voxel correctly. However, most of the occurring problems can be removed by appropriate postprocessing. First, we set $B^*_{\text{extrema}}(x, y, z) = 0$ if $I(x, y, z) < \tau$, where τ is a manually chosen threshold. Then we remove small isolated clusters of foreground voxels by applying two 2D rank order filters. More precisely, a foreground voxel is assigned to the background if the ratio of voxels classified as foreground within a sphere of radius r is smaller than α (here: $r_1 = 2, \alpha_1 = 0.5$ and $r_2 = 10, \alpha_2 = 0.15$). Finally, we perform a dilation by a 2D disk with radius $r_{\text{dil}} = 4.5$, which is limited to voxels with a grey intensity in the original image I above the previously chosen threshold τ. This dilation connects otherwise separated voxel to a large set of connected regions and provides the final outcome of our approach. Fig. **??** provides an illustration for all postprocessing steps.

In the first two steps, the parameter τ and the corresponding radii $r_{1/2}$ and quantiles $\alpha_{1/2}$ for the rank order filters are chosen to provide a good optical fit. The parameter r_{dil} for the dilation, which is the most influencual step, is chosen to match the original volume fraction of the material, which

is a commonly known property of most specimen.

4. Results

We now present the segmentation results, which have been obtained by our algorithm, and compare them to those of a global thresholding and a manual segmentation. The manual segmentation was performed by first applying a certain global threshold and then manually correcting the images using the software gimp [11]. Furthermore, a local thresholding approach has been tested. However the best results were obtained for a window size equal to the dimension of the image, i.e., it turned out that the best local thresholding is identical with global thresholding.

4.1. Visual Comparision of Segmented Images

A visual comparison of 2D slices (see Fig. **??**) indicates a significant improvement which has been achieved by the automatic segmentation algorithm proposed in Section 3. This is also reflected by the rate of errounously classified voxels, which was reduced to 16.7% (thresholding 22.5%), supposing that the manual segmentation is correct. Both phases are now being detected by a probability above 80%, with background voxels being detected more often (85.7%) than foreground voxels (80.7%). Visual inspection shows

that some of the missing foreground voxels are false positives in the manual segmentation, which is, due to the huge time consumption, always limited in detail. For more information, see Table 1, where the rates for correct and wrong classification of foreground and background voxels, respectively, are given, comparing the results of manual segmentation with those of automatic segmentation as proposed in Section 3.

Although the rates given in Table 1 show a clear advantage of the segmentation approach proposed in this paper relative to global thresholding, they do not fully capture the improvement which has been achieved with respect to correct reconstruction of the 3D morphology. Within the context of material structure, the preservation morphological features is more relevant than the correct classification of individual voxels. Therefore, we will give a more structurally oriented comparison in the following section.

4.2. Spherical Contact Distribution Function

The spherical contact distribution function (SCDF) is a common tool in stochastic geometry to compare the 3D morphologies of random sets [15]. For binary image data, the empirical SCDF is given by the cumulative distribution function of the distances of all background (foreground) voxel to their nearest foreground (background) voxel, respectively. Fig. **??** shows the em-

pirical SCDF of both background and foreground for the three segmentation approaches considered in this paper. In both cases the result provided by the automatic segmentation algorithm proposed in this paper is significantly closer to the empirical SCDF of the manual segmentation than that corresponding to thresholding. Note that a lower rate of missclassified voxels does not necessarily lead to a better fit of the corresponding SCDF. Depending on the spatial distribution fewer voxels might even have a stronger negative impact on the structure. For a network of closed pores, for example, an overestimation of the overall pore sizes by 10% might not be as severe as classifying 5% of the pores as open, although they are closed. The same is true for the SCDF were background (foreground) voxels in the center of regions otherwise classified as foreground (background) have a stronger impact than voxels close to the border of such regions. Such structural differences have a direct link to the properties of the corresponding material such as its performance in its respective application.

Furthermore, two difference images have been analysed which were constructed by voxel-wise comparison of the manually segmented image with the automatically segmented image and the image obtained by global thresholding, respectively. The empirical SCDF of these two difference images are

visualized in Fig. **??**. They show that in the automatically segmented image more than half of the misclassified voxels have a correctly classified neighbour and, therefore, are presumed not to have a larger impact on the morphological properties of the image. The main difference between the binarisation obtained by the new approach proposed in this paper and global thresholding occurs for greater radii between 2 and 6. Agagin, this suggests that the new approach preserves significantly more features of the original 3D morphology.

4.3. Additional Data Sample

In the following we describe the result obtained by our algorithm for another image. This image shows a monolithic foam-like silica material (see Fig. **??**) and was previously studied in [1]. In this case, however, our primary goal is not to obtain a reasonable segmentation for later analysis but to test the applicability of our new approach to other scenarios and the plausibility of its assumptions. We chose this particular image because it exhibits various characteristics that are different to the image studied so far. This includes different levels of illumination across the image and significantly different structural properties of the material. The foam-like structure mostly consists of spherically shaped pores that are enclosed by thinner cell walls. This

structure leads to a scenario with significantly different characteristics for the corresponding z-profiles, which are analysed by the key part of our algorithm.

The preprocessing was performed as described in [1] with an additional hMinima-transform applied to each z-profile. For more details on hMinima-transform see [16]. This smoothed the z-profiles leading to more robust results. However, the definition of local minima had to be changed to include plateaus, where a voxel (x, y, z) is also considered a local minima if its gray intensity is $\leq$ (instead of a strict $<$) than it's neighbouring voxels. Furthermore, we used a different set of parameters for both the key-algorithm ($\tau_{\max} = 20, \tau_{\min} = 35$) and for postprocessing ($\tau(x) = \text{mean}_{r=10}(I)(x) + 5, r_1 = 2, \alpha_1 = 0.2, r_2 = 1, \alpha_2 = 0, r_{\text{dil}} = 3$). Note that the threshold τ is no longer location-independent and that only one rank order filter was used.

With this setup the approach is capable of obtaining a reasonable segmentation for the additional data set. However, unlike in Section 4.2, we are not able to perform a quantitative comparison due to the lack of a reference segmentation. Visual inspection however shows that most features are preserved and the quality of the result is similar to the one presented in [1]. A general trend seems to be that cell walls appear thinner with the new approach, which is an improvement to the previously overestimated thickness of

cell walls. This effect also supports the introduction of a separate detection of the first appearance of structures. On the down-side some structures that are present for the approach from [1] seem to be missing (or incomplete). This seems to be a trade-off for the reduced amount of false positives, i.e., structures that were present in the segmentation by the previous approach although they don't have a corresponding counterpart in the gray-scale image.

5. Conclusion

We have proposed a new approach to automatic segmentation of FIB-SEM images. This approach was developed by following the key-principle of analysing the variation of grey intensities in z-direction which has recently been considered in [1]. Therefore, we introduced the notions of error-tolerant local maxima and minima and introduced threshold criteria to distinguish them from (smaller) extrema within substructures. These local maxima and minima then are used as an indicator for the beginning and end of substructures, respectively. From this preliminary segmentation we derived a final binarisation by some postprocessing which consists of a thresholding, cluster-detection and dilation. The final result was then analysed and compared with those obtained by manual segmentation and global thresholding.

Besides a visual and quantitative evaluation this analysis also covered a structural analysis of the obtained segmentations and the missclassified voxels. It turned out that the segmented image, which has been obtained by the new approach considered in this paper, preserves significantly more features of the original 3D morphology than this is possible by global thresholding. We have also described why we consider this to be even more relevant than mere numbers of misclassified voxels. Finally our approach was applied to a second image, where it also obtained a reasonable segmentation, suggesting that this approach will be applicable to a range of scenarios with variable properties. However, in spite of the advances of the present approach there is still work to be done on the way towards more robust and reliable segmentation approaches.

[1] M. Salzer, A. Spettl, O. Stenzel, J.-H. Smått, M. Lindén, I. Manke, V. Schmidt, A two-stage approach to the segmentation of fib-sem images of highly porous materials, Materials Characterization 69 (0) (2012) 115–126.

[2] S. Dunn, Hydrogen futures: toward a sustainable energy system, International Journal of Hydrogen Energy 27 (2002) 235–264.

[3] Y. Shao, J. Liu, Y. Wang, Y. Lin, Novel catalyst support materials for pem fuel cells: current status and future prospects, Journal of Materials Chemistry 19 (2008) 46–59.

[4] M. Mezedur, M. Kaviany, W. Moore, Effect of pore structure, randomness and size on effective mass diffusivity, AIChE Journal 48 (2002) 15–24.

[5] N. Siddique, F. Liu, Process based reconstruction and simulation of a three-dimensional fuel cell catalyst layer, Electrochimica Acta 55 (19) (2010) 5357–5366.

[6] L. Holzer, F. Indutnyi, P. Gasser, B. Munch, M. Wegmann, Three-dimensional analysis of porous $BaTiO_3$ ceramics using FIB nanotomography, Journal of Microscopy 216 (2004) 84–95.

[7] G. Gaiselmann, M. Neumann, L. Holzer, T. Hocker, M. R. Prestat, V. Schmidt, Stochastic 3D modeling of $La_{0.6}Sr_{0.4}CoO_{3-\delta}$ cathodes based on structural segmentation of FIB-SEM images, Computational Materials Science 67 (2013) 48–62.

[8] T. Hutzenlaub, S. Thiele, R. Zengerle, C. Ziegler, Three-dimensional

reconstruction of a $LiCoO_2$ Li-ion battery cathode, Electrochemical and Solid-State Letters 15 (2012) A33–A36.

[9] O. Stenzel, D. Westhoff, I. Manke, M. Kasper, D. Kroese, V. Schmidt, Graph-based simulated annealing: A hybrid approach to stochastic modeling of complex microstructures, Modelling and Simulation in Materials Science and Engineering 21 (2013) 055004.

[10] C. Ziegler, S. Thiele, R. Zengerle, Direct three-dimensional reconstruction of a nanoporous catalyst layer for a polymer electrolyte fuel cell, Journal of Power Sources 196 (4) (2011) 2094–2097.

[11] S. Thiele, R. Zengerle, C. Ziegler, Nano-morphology of a polymer electrolyte fuel cell catalyst layer–imaging, reconstruction and analysis, Nano Research 4 (2011) 849–860.

[12] E. Wargo, T. Kotaka, Y. Tabuchi, E. Kumbur, Comparison of focused ion beam versus nano-scale x-ray computed tomography for resolving 3-d microstructures of porous fuel cell materials, Journal of Power Sources 241 (0) (2013) 608 – 618.

[13] S. Thiele, T. Fürstenhaupt, D. Banham, T. Hutzenlaub, V. Birss, C. Ziegler, R. Zengerle, Multiscale tomography of nanoporous carbon-

supported noble metal catalyst layers, Journal of Power Sources 228 (0) (2013) 185–192.

[14] T. Sarjakoski, J. Lammi, Least square matching by search, Proceedings of the XVIII ISPRS Congress Vienna Austria XXXI (1996) 724–728.

[15] S. N. Chiu, D. Stoyan, W. S. Kendall, J. Mecke, Stochastic geometry and its applications, J. Wiley & Sons, Chichester, 2013.

[16] J. Ohser, K. Schladitz, 3D Images of Materials Structures: Processing and Analysis, Wiley-VCH, Weinheim, 2009.

Tables

classified as	FG manually	BG manually
FG automatic	80.7%	14.3%
(FG thresholding)	(71.5%)	(18.2%)
BG automatic	19.3%	85.7%
(BG thresholding)	(28.5%)	(81.8%)

Table 1: Detection rates for foreground (FG) and background (BG) voxels. By detection rate we denote the probability that a voxel is classified as foreground or background by the automatic approach (rows) given that it was classified as foreground or background by the manual approach (columns). Thus, the diagonal elements provide the amount of correctly classified voxels and the off-diagonal elements the falsely classified voxels. In brackets the corresponding rates are given for the comparision of manual segmentation and global thresholding.

Figures

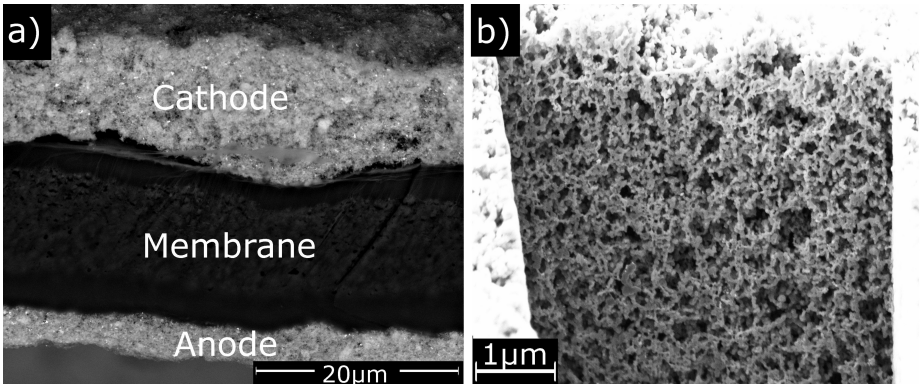

Figure 1: Membrane electrode assembly with cathode, anode and membrane (a); cavity in the cathode opened by FIB (b)

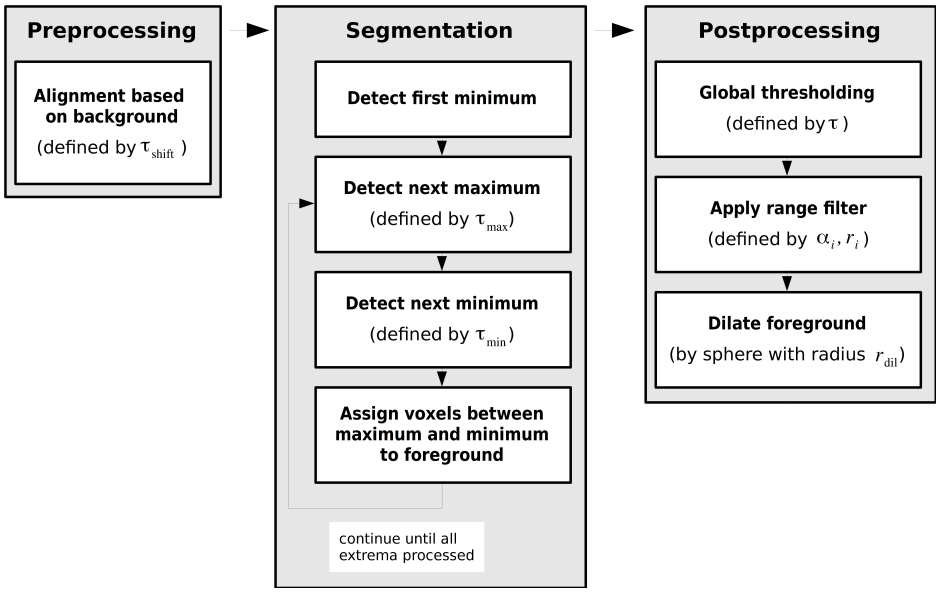

Figure 2: Flow chart of the steps performed during the segmentation process including the required parameters for these steps

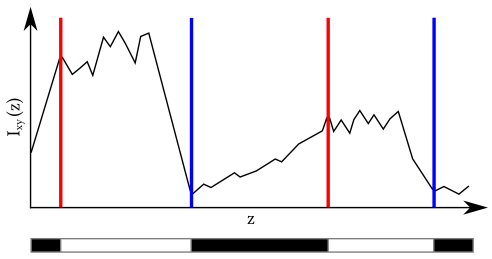

Figure 3: Schematic 1D example for the detection of local maxima (red) and minima (blue). The bar below shows the binarised image

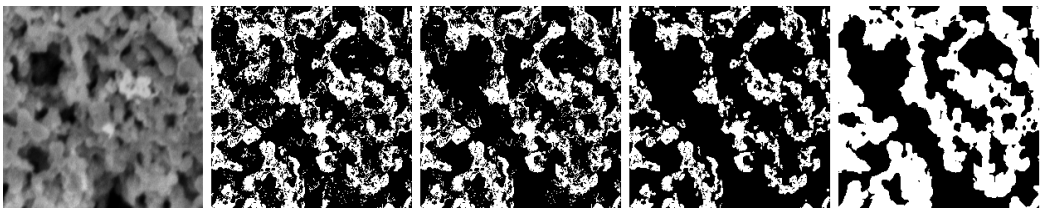

Figure 4: Visual example of the effect of postprocessing. From left to right: original grayscale image I; segmentation before postprocessing; after removing foreground voxels with gray intensity $I(x) < \tau$; after removing isolated clusters based on their rank order; dilation (limited to voxels with $I(x) > \tau$) and final result

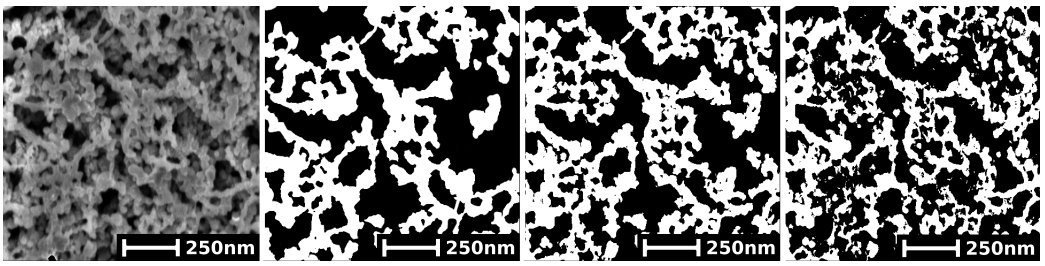

Figure 5: A visual example for the results of different segmentation results. From left to right: original grayscale image; manual segmentation; automatic segmentation as stated in this paper; global thresholding

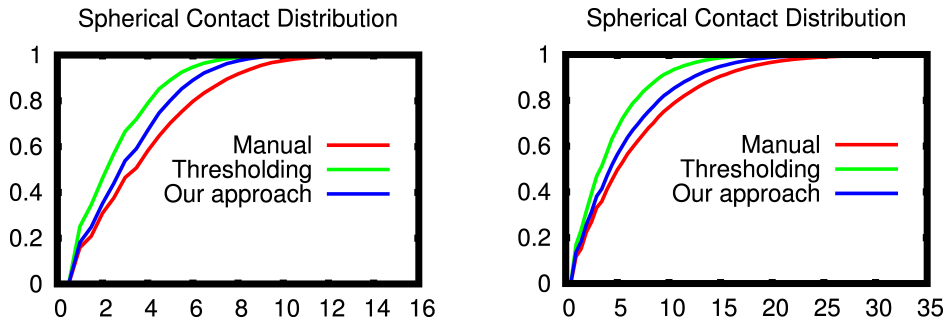

Figure 6: Empirical SCDF for foreground (left) and background (right) for all three segmentation approaches. In both cases the result of our approach is significantly closer to the manual segmentation than the result of global thresholding.

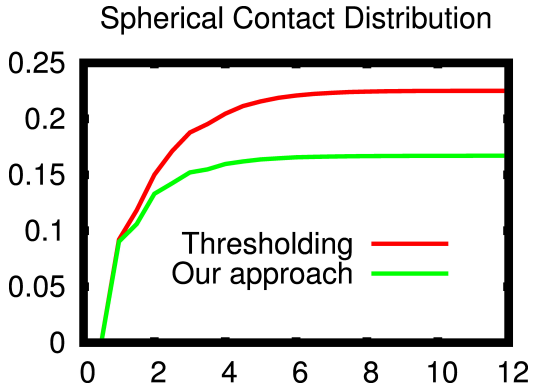

Figure 7: Empirical SCDF for an image containing the differences between the automatic segmentation and the manual segmentation. For global thresholding there is a significant increase after a voxel size of 4. This increase is much smaller for our approach which indicates that the amount of bigger clusters of missclassified voxels is reduced significantly.

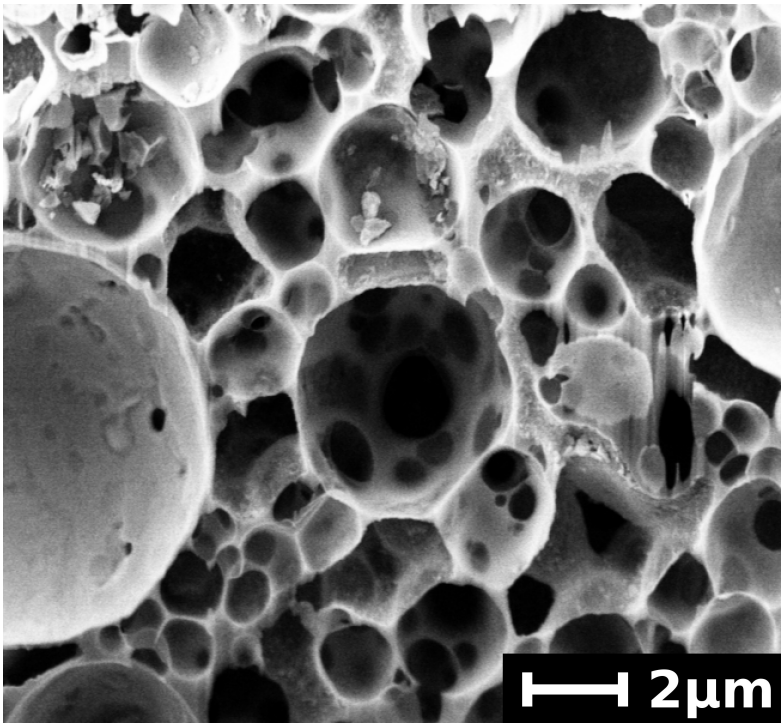

Figure 8: 2D slice from the 3D FIB-SEM image showing a foam-like silica material. The structure of the pore space leads to a different configuration of artefacts, e.g., different levels of illumination for different pore sizes.

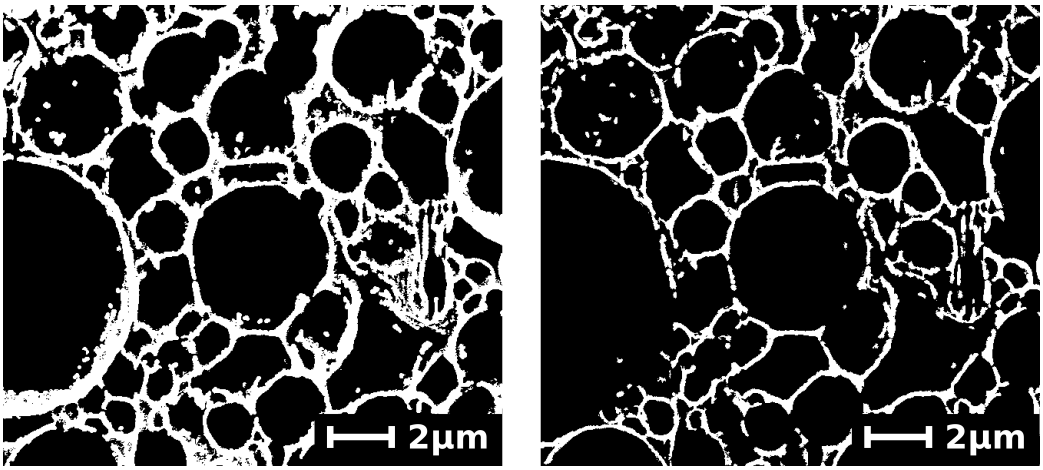

Figure 9: Binarisation results for a foam-like silica material (see Fig. **??** for the grayscale version). On the left: result obtained by our new approach. On the right: result of the method described in [1] as a reference. Most structures are preserved by both methods. For our new approach there seem to be more structures missing (e.g. cell walls open), while for the old approach there is the tendency to overestimate present structures (e.g. thicker cell walls) and to show additional ones.